Metastability, nanocrystallinity and pseudo-solid solution effects on the understanding of schwertmannite solubility

Manuel A. Caraballo[1,2,3] *, J. Donald Rimstidt[1], Francisco Macías[2], José Miguel Nieto[2] and Michael F. Hochella Jr.[1].

1 Department of Geosciences, Virginia Tech, 4044 Derring Hall, Blacksburg, Virginia, 24061, USA

2 Geology Department, University of Huelva, Campus "El Carmen", E-21071 Huelva, Spain

3 Mining Engineering Department, University of Santiago, Avda. Tupper 2069 Santiago, Chile

---

* Corresponding author. Tel.: +1-540-267-5383; fax: +34-95-921-9810

E-mail address: manuelac@vt.edu (Manuel A. Caraballo)

Abstract

The role of metastable nanocrystalline precursors, like schwertmannite, in iron and sulfate rich acidic waters is commonly underestimated or even neglected. In addition to schwertmannite metastability, its heterogeneous chemical composition and the current use of disparate solubility products results in an incongruous understanding of this mineral. In order to characterize schwertmannite stability in acid mine drainage settings, we used coincident schwertmannite and solution samples to determine how its solubility product is related to its composition. The solubility products (as log K_{sp}) for 30 natural samples of this study span a range of log K_{sp} values from 5.8 to 39.5. These values show a gradual distribution on the pH-pe space from pH 1.93 to 4.71 and pe values from 8.5 to 13.7. A set of three predictive equations to select the best schwertmannite solubility product for each new specific case study was obtained. This approximation allows generating an appropriate solubility product for schwertmannite despite the lack of information in certain environments (e.g., absence of former water chemistries on Mars). The trend observed for Fe and S content in schwertmannite can be interpreted as a pseudo-solid solution ranging from high to low S and Fe concentrations. The polyphasic nature of schwertmannite was studied by means of a thermodynamic model assuming equilibrium between a hydrous ferric oxide (HFO), schwertmannite, and solution. All the results obtained in this study support the understanding of schwertmannite as a polyphasic nanomineral and encourage using a broad log K_{sp} range to reproduce the solubility of schwertmannite in nature.

Keywords

Acid mine drainage, schwertmannite, solubility product, polyphasic nanomineral.

1. Introduction

Surficial iron rich waters often precipitate the Fe-bearing nanominerals ferrihydrite and schwertmannite (Banfield and Zhang, 2001). The study of Fe-bearing nanominerals and mineral nanoparticles is being considered from many different angles, including: crystal growth by oriented attachment (Li et al., 2012), size-driven thermodynamic complexity (Navrotsky et al., 2008), catalytic and sorption processes (Madden and Hochella, 2005) and environmental pollutant transport (Hassellov and von der Kammer, 2008; Plathe et al., 2013). However, an understanding of the connection between water chemistry and nanominerals solubility and bulk composition can help to tie together these approaches.

Acidic waters rich in sulfate and iron control an important part of the iron cycle under Earth-surface conditions. Acid mine drainage (AMD) is the primary example of these types of waters. AMD is the result of the interaction between sulfides (mainly pyrite), water and air. AMD water chemistry is greatly influenced by jarosite, schwertmannite and ferrihydrite solubilities at very low (1.5-2.5), low (2.5-5.5) and intermediate (>5.5) pHs (Bigham et al. 1996), respectively; however there is not a consensus about the extent of the solubility field for each of these three mineral phases and quite disparate pH ranges and solubility products have been proposed (Cornell and Schwertmann, 2003; Majzlan et al., 2004). Notwithstanding, schwertmannite has been proposed as a metastable iron mineral controlling iron precipitation, and concomitantly water chemistry, over a wide range of pH (Bigham et al., 1996; Bigham and Nordstrom, 2000; Majzlan et al, 2004). Three quite different log K_{sp} values for schwertmannite are commonly accepted and used indiscriminately to model schwertmannite solubility, namely: 7.06 ± 0.09 (Kawano and Tomita, 2001), 10.05 ± 2.5 (Yu et al., 1999) and 18.0 ± 2.5 (Bigham et al., 1996).

Schwertmannite is widely present in acidic sulfate and iron rich waters (Bigham and Nordstrom, 2000) and is a metastable precursor leading to jarosite or goethite formation (Acero et al., 2006). Apart from the well-known locations in mine districts in association with AMD (pit lakes, underground galleries, spoil heaps, tailings and rivers), schwertmannite has been reported in a broad variety of other environments such as acidic soils (Burton et al., 2008), gossan deposits in artic environments (West et al., 2009), intertidal marshes (Johnston et al., 2011) and oxic microenvironments beneath polar glaciers (Raiswell et al., 2009). Schwertmannite has also been reported to play an essential role in toxic metal removal (mainly arsenic), in AMD passive remediation systems (Macías et al., 2012; Caraballo et al., 2011).

Recent studies suggest the presence of schwertmannite on Mars and as a precursor to the Banded Iron Formations (BIF) generated during Precambrian times. After the presence of schwertmannite was suggested as a component in Meridiani outcrop materials (Farrand et al., 2009) and the Meridiani Planum region (Bibring et al., 2007), it has become a keystone mineral phase in several recent studies that model the current mineral composition of the Martian surface. These models incorporate schwertmannite as a metastable precursor to other mineral phases like jarosite or goethite (Marion et al., 2008; Tosca et al., 2008; Hurowitz et al., 2010). In the case of the BIFs, ferrihydrite is unanimously accepted as a precursor of goethite (and finally hematite) in the seawaters generating these sediments (Hoashi et al, 2009). Based on Mo-Rh (Anbar et al., 2007), Ni (Konhauser et al., 2009) and Cr (Konhauser et al., 2011) concentrations in the rocks forming BIFs today, some studies have proposed the oxidative weathering of crustal sulfide minerals (and the concomitant generation of acidic iron and sulfate rich waters) as a mechanism increasing the concentration of sulfate in Precambrian seawaters. This new theory opens an exciting research area where a better understanding of schwertmannite solubility is essential to understand the control that this “paleo-AMD” could have in the generation of some very specific formations corresponding to shallow-water deposits like the Granular Iron Formations (Konhauser et al., 2011).

The growing awareness of the influence of Fe-bearing nanominerals, particularly schwertmannite, in the hydrochemistry of present and past Earth and Mars environments, calls for a better understanding of how their solubility is controlled by water chemistry, mineral crystallinity, and aggregation state. The goal of this study is to unify our knowledge of schwertmannite solubility and composition using a new approach.

2. Methods

Compositional data for coexisting schwertmannite and natural waters were obtained from hydrochemical and mineral field samples. These data were supplemented with data from the literature. It is important to emphasize that the current study is focused on schwertmannite samples formed under natural conditions. Therefore, the use of any bibliographic information involving synthetic schwertmannite samples, produced by titration (or by any other method) of synthetic or natural AMD waters, has been purposely and necessarily excluded from our analyses, calculations, and conclusions despite its great value in the general understanding of this material.

The current research follows the path opened by pioneering studies in this subject (Bigham et al., 1996; Yu et al., 1999) which require: 1) schwertmannite precipitation in a system close to equilibrium, and 2) working with schwertmannite samples that have no other Fe minerals present. As shown in the following sections, many strict limitations have been imposed on the sampling methods used in this particular study in order to comply with these two fundamental requirements. Unfortunately, some inherent limitations of this approach can not be completely ruled out, among them: 1) natural solutions in contact with schwertmannite may be slightly different from the solutions present during the growth of the original schwertmannite due to hydrochemistry evolution, 2) the existence of a possible kinetic barrier for schwertmannite precipitation may require some degree of oversaturation before precipitation, and 3) compositional factors inhibiting or enhancing mineral precipitation (e.g., organic matter). Nevertheless, the restrictive methodology employed in the present study offers a reliable and robust foundation to address the study of natural schwertmannite solubility.

2.1. Field sampling

Field sampling was carried out within the Iberian Pyrite Belt (IPB), SW Spain. This region suffers ubiquitous and severe AMD pollution due to more than a remarkable five millennia of mining activity (Nocete et al., 2005). The iron- and sulfate-rich acidic waters show wide variations in physicochemical parameters and water compositions making our field data set representative of a wide range of conditions where schwertmannite forms in AMD (Sarmiento et al., 2009).

Two extensive field campaigns in 2010 and 2011 yielded 20 samples. At each site, solutions were sampled in the vicinity of the schwertmannite precipitates or directly from the waters containing colloidal schwertmannite samples. The solutions were filtered immediately after collection through 0.1 μm Millipore filters, acidified in the field to $pH < 1$ with suprapur HNO_3, and stored at 4 ºC in 60 mL sterile polypropylene containers until analysis. The unequivocal presence of schwertmannite as the only mineral phase in the precipitates in contact with the AMD was imposed to (1) ensure that the waters were close to equilibrium with schwertmannite and rule out the possibility that the presence of jarosite or goethite might influence the calculated solubility products, and (2) to guarantee that the chemical composition of the solid correspond exclusively to schwertmannite. Only nine of the 20 initial samples satisfied these restrictions (Fig. 1 and Table 1).

2.2. Bibliographic sampling

A total of 20 publications with more than 60 potential "bibliographic" sampling points were selected from the extensive peer-reviewed literature available. However, this information was refined by requiring that the solution and solid be sampled at the same time and place, specification of the field pe values or Fe speciation (Fe^{+3}-Fe^{+2}) was required, the solution charge balance error was limited to less than ±15%, and schwertmannite had to be the only Fe-bearing mineral phase comprising the solid sample.

The final data set contained nine field-derived data from the IPB plus 21 "bibliographic" sampling data (n=30) from around the world, as shown in Table 1. An additional data set (Electronic Annex A, Table A1, n= 46) was specifically generated to study the Fe and S content in schwertmannite. Due to the very specific purpose of this complementary dataset it was not necessary to apply any restriction to the collection of these data beyond the existence of S and Fe concentrations for each pure, natural schwertmannite sample.

All the "bibliographic" schwertmannite samples used in this study are described in publications where the presence of pure schwertmannite was not only claimed but also specifically shown by means of an XRD pattern. In addition, most of these studies also used between two and four other complementary analytical techniques to certify the presence of only schwertmannite, including: Fourier transform infrared spectroscopy (FTIR), scanning electron microscopy (SEM), high resolution transmission electron microscopy (HRTEM), x-ray photoelectron spectroscopy (XPS), Mössbauer spectrometry, differential thermal gravimetry (DTG), and sequential extractions.

2.3. Analytical methods

Water pH and redox potential were measured in the field using a PH25 meter (Crison®) with Crison electrodes. Redox potential and pH were calibrated using 2 points (240–470 mV) and 3 points (pH 4.01–7.00–9.21), respectively, with Crison standard solutions. Redox potential measurements were corrected to the Standard Hydrogen Electrode to calculate pe.

Concentrations of dissolved Al, As, Ba, Be, Ca, Cd, Co, Cr, Cu, Fe, K, Li, Mg, Mn, Na, Ni, S, Si, Sr, Ti, V and Zn were determined by Inductively Coupled Plasma Atomic Emission Spectrometry (ICP-AES Jobin- Ybon Ultima2) using a protocol especially designed for AMD samples (Tyler et al., 2004).

The predominance of schwertmannite in the solid samples was confirmed by powder X-ray diffraction (XRD) of randomly oriented powder samples. This analysis exercise performed using a Bruker D5005 X-ray diffractometer with Cu*K*α radiation. Diffractometer settings were: 40 kV, 30 mA, and a scan range of 2–65° 2θ, 0.05 °2θ step size, and 20 s counting time per step. Solid samples bulk chemistry was analyzed by ICP-AES after digesting the samples with concentrated HNO_3 at room temperature.

The speciation of the water chemistry as well as the charge balance for all the samples was calculated using the equilibrium geochemical speciation/mass transfer model PHREEQC (Parkhurst, 1995) using the database of the speciation model MINTEQ (Ball and Nordstrom, 1991).

The study of the statistical distribution of variates in Table 1, the possible correlations between them as well as the multiple regression model fit for the solubility product constant of schwertmannite was performed with JMP®9.0.1 statistical software.

3. Results

3.1. Defining the hydrochemical and compositional ranges generating schwertmannite in nature

AMD waters generating schwertmannite, based on the observations made in this study, are characterized by a pH and pe distribution ranging from a pH of 1.93 to 4.71 and a pe of 8.50 to 13.70 (Fig. 2 and Table 1). The highest density of values for these two parameters is in the region of pH 3.02 ± 0.56 and pe 11.37 ± 1.37. The activities of ferric iron and sulfate are distributed within significantly different ranges, with log $a_{Fe^{3+}}$ covering almost four orders of magnitude while log $a_{SO_4^{2-}}$ is restricted to values within the same order of magnitude (Fig. 2 and Table 1). An additional idea of iron and sulfate distribution in these waters can be obtained from the broad distribution of the concentrations of these two elements ranging from 0.03-18.89 mmol/L Fe and 7.40-97.34 mmol/L SO_4^{2-} (Table 1).

The molar ratio of the Fe and S concentrations in the solid is commonly used to characterize the composition of schwertmannite. A Fe/S_{molar} range spanning from 4 to 8 is typically accepted for schwertmannite (Bigham and Nordstrom, 2000). However, this range was proposed using the available data from the 1990s. The inclusion in the current work of many other recent schwertmannite studies allows for a more robust and comprehensive database. As can be observed in figures 2 and 3B, schwertmannite Fe/S_{molar} ratios show a high sample population region between 4 and 6, while overall spanning a broader region going from 3.77 to 15.53.

According to schwertmannite stoichiometry in equation 2, any change *x* in SO_4^{2-} concentration is compensated by an *8-2x* change in OH^- concentration, and therefore a change in schwertmannite mass is expected. However, for the range of *x* values typically found in nature (from 0.5 to 2), the variations in the theoretical mass of schwertmannite as a result of SO_4^{2-} and OH^- exchange can be considered negligible (< 1%). If Fe and S concentrations (mmol of element/ g of schwertmannite) are plotted against each other, the data can be fitted by a line with the following equation (Fig. 3A):

$$Fe = 4.41(0.245) + 1.94(0.196)S \qquad (n = 46,\ R^2 = 0.690) \tag{1}$$

The numbers in parentheses correspond to the standard error for each parameter.

The variates comprising the data set of this study were subjected to a correlation study and the Pearson correlation coefficients obtained are displayed in Table A2 (Electronic Annex A). The correlations obtained are typical of AMD environments so there is not any new information to show in this section. However, a brief explanation of the results is offered in Electronic Annex A.

3.2. Solubility product calculations

The solubility product of each schwertmannite sample was calculated using the modeled ion activities listed in Table 1. To this end, the general formula for schwertmannite proposed by Bigham et al., 1994 was employed. This formula, based on an akaganéite-type structure, was designed to accommodate the Fe to S molar ratios and OH concentrations observed in natural schwertmannite samples and therefore can be considered to date as the best option to summarize schwertmannite solubility in natural samples. Based on the Bigham formula, the schwertmannite congruent dissolution reaction is:

$$Fe_8O_8(OH)_{8-2x}(SO_4)_x + (24-2x)H^+ = 8Fe^{3+} + xSO_4^{2-} + (16-2x)H_2O \qquad (2)$$

This means that the solubility product can be calculated as:

$$\log K_{sp} = 8\log a_{Fe^{3+}} + x\log a_{SO_4^{2-}} + \left(24-2x\right)pH \qquad (3)$$

where x corresponds to the stoichiometric SO_4^{2-} (obtained after calculating the measured SO_4^{2-} content in each schwertmannite on the basis of 8 Fe atoms). Log $a_{Fe^{3+}}$ and log $a_{SO_4^{2-}}$ are the activities of ferric iron and sulfate calculated from the measured concentrations and pe (Table 1).

The log K_{sp} values range from 5.8 to 39.5 (Fig.2 and Table 1), including within this range the three log K_{sp} for schwertmannite that are widely quoted in the literature, namely: 7.06 ± 0.09 (Kawano and Tomita, 2001), 10.05 ± 2.5 (Yu et al., 1999) and 18.0 ± 2.5 (Bigham et al., 1996).

4. Discussion

4.1. Schwertmannite solubility

In AMD affected water, pH and pe can be considered the most important variables controlling both metal speciation and mineral precipitation. The use of pe-pH predominance diagrams offers a simplistic, but at the same time reliable visualization of mineral phases and dissolved species distribution under various hydrochemical conditions. It allows establishing predominance areas where a certain mineral or aqueous species is expected to be present due to its high activity (compared with other phases or species). However, it is worth remembering that the boundaries of predominance diagrams represent conditions under which the activities of phases or species predominating in two adjoining fields are equal. Therefore, phases or species can also be stable beyond their predominance region, but they will not be dominant.

Schwertmannite is known to be a metastable precursor of both jarosite and goethite (Acero et al., 2006), whereas ferrihydrite has been observed to be metastable with respect to goethite (Cornell and Schwertmann, 2003); therefore, in order to generate a realistic pe-pH predominance diagram for Fe-S-K-O-H system at 298 K and 1 bar, it was decided to take the following approach:

1) Generate a pe-pH predominance diagram for the main stable mineral phases (jarosite, goethite and pyrite) and the most relevant iron and sulfur species involved in the equilibrium reactions with those minerals (Fig. 4A).

2) Plot the pe and pH values of the schwertmannite samples from this study on the top of the previously generated pe-pH predominance diagram and define the extension of the schwertmannite predominance field. To this end, the calculated solubility products (as log K_{sp}) for each sample were also shown to study their distribution in the pe-pH space and select the most representative ones to calculate the different boundaries confining the schwertmannite meta-stability predominance field (Fig. 4B).

The final pe-pH predominance diagram for the Fe-S-K-O-H system at 298 K and 1 bar (Fig. 4C) was obtained by overlapping the two previous partial diagrams in figure 4. The specifics for the calculations of these diagrams are offered in Electronic Annex B.

Schwertmannite and ferrihydrite are kinetically favored (relative to goethite) in AMD and typically serve as mineral precursors for goethite. Taking this into account, the final pe-pH predominance diagram confines the preponderance of goethite to a very narrow region between predominance areas for schwertmannite and ferrihydrite on the top and dissolved species on the bottom (Fig. 4C). It is also worth noting that, to the best of our knowledge, goethite direct precipitation in nature has not been reported for the range of pH (from approx. 2 to 5) and temperature (298 K) covered in this study. Therefore, the appearance of the very limited goethite preponderance field (Fig. 4C) may be due to the fact that the corresponding schwertmannite and ferrihydrite specimens have yet to be reported.

The schwertmannite predominance field is expanded to both higher and lower pHs compared with previously reported values (Bigham et al., 1996; Majzlan et al., 2004). The distribution and extension of these predominance fields better reproduce the typically observed neoformed mineralogy in Fe-SO_4^{2-} rich acidic waters within AMD environments.

The wide and progressive variation of log K_{sp} with pH and pe (Fig. 4B) strongly suggests that it should not be modeled as a single value, but rather schwertmannite should be treated as having a solubility product that varies with the sulfate content of the mineral as suggested by equations (2) and (3).

To facilitate the selection of the most appropriate log K_{sp} defining schwertmannite solubility, a predictive statistical tool was generated. The variates included in the model (pH, log $a_{Fe^{3+}}$, log $a_{SO_4^{2-}}$ and x) were the same employed to generate each single log K_{sp} in this study (Eq. 2). The following equation line was obtained:

$$\log K_{sp} = 11.51(0.803) + 20.79(0.271)pH + 7.81(0.188)\log a_{Fe^{3+}} + 1.42(0.313)\log a_{SO_4^{2-}} - 8.01(0.146)x \qquad (n = 30,\ R^2 = 0.998) \tag{4}$$

The numbers in parenthesis correspond to 1 standard error of each parameter.

The former predictive model can be split into two equations accounting just for the water related variates (w-model) or the solid related variate (s-model). When the w-model is used to obtain schwertmannite log K_{sp}, the correlation observed is slightly weaker:

$$\log K_{sp} = -1.980(8.27) + 18.76(2.91)pH + 5.57(1.98)\log a_{Fe^{3+}} + 3.22(3.37)\log a_{SO_4^{2-}} \qquad (n = 30,\ R^2 = 0.811) \tag{5}$$

A good correlation between log K_{sp} and xSO$_4^{2-}$ values (s-model) is only obtained after filtering some outlier values (e.g., x = 2.58 from Regenspurg et al., 2005) and some extreme values maintained in the general model (e.g., log K_{sp} = 39.5 and 5.8, this study).

Taking into account these limitations, the following statistical predictive equation is proposed for the s-model:

$$\log K_{sp} = 40.40(3.47) - 15.10(2.27)x \quad (n = 23,\ R^2 = 0.68) \tag{6}$$

The reproducibility of the log K_{sp} obtained with these three approximations is offered in Table 2. As shown, the modeled log K_{sp} values obtained from equation 4 perfectly reproduce the real values calculated in this study. The more simplistic approaches in equations 5 and, mainly, in equation 6 imply a lower reproducibility for the predicted log K_{sp} (Table 2). Notwithstanding, they allow generating an acceptable schwertmannite log K_{sp} very close to the real value. These last two equations can play an essential role in very important Earth and planetary environments where the required information to generate log K_{sp} values using equation 3 are unavailable (e.g., absence of the original water chemistry on the Martian surface or lack of solid composition in certain studies modeling acidic waters).

4.2. Schwertmannite pseudo-solid solution

Schwertmannite was accepted as a new mineral phase (with an akaganéite-type crystalline structure) in 1994 (Bigham et al., 1994). However, schwertmannite is well known to be very poorly crystalline, meta-stable with respect to goethite and jarosite (Acero et al., 2006), and significantly variable in its solubility and bulk composition (Cornell and Schwertmann, 2003). These singular characteristics have opened questions about the current use of a relatively fixed stoichiometry and crystal structure to define this mineral. Recent work using synchrotron-based techniques (Fernández-Martínez et al., 2010) has interpreted schwertmannite in the terms of a traditional "akaganéite-type" structure whereas some other studies using HRTEM in synthetic (Hockridge et al., 2009) and natural samples (French et al., 2012) suggest that schwertmannite should not be considered a single mineral with a repeating unit cell, but as a polyphasic nanomineral comprising nanocrystals of hydrous ferric oxide (HFO) phases (ferrihydrite or goethite) surrounded by a sulfate rich amorphous matrix.

The trends observed for Fe and S content in schwertmannite (Fig. 3A and B), as well as the wide range in the Fe/S molar ratio that this mineral shows in nature (Fig. 2 and Tables 1 and A1), reflect a compositional behavior that could be understood as a pseudo-solid solution. As can be observed, this trend does not reproduce a real solid solution with two distinctive end members where two elements are interchanged on a determined structural position. Indeed, the concentrations of Fe and S in schwertmannite clearly define a coupled tendency for both elements, progressively moving from high Fe and S concentrations to low Fe and S concentrations or vice versa (Fig. 3A). In addition, if the Fe/S molar ratio is compared with the S content in the samples (Fig. 3B), it can be observed how the Fe/S molar ratio increase following a polynomial trend as the S content of the samples decrease.

The important variations on schwertmannite S content have been commonly attributed to different amounts of SO_4^{2-} adsorbed to the mineral surface (Caraballo et al., 2009). However, bearing in mind the recent discovery of HFO nano-domains within schwertmannite nanoparticles (French et al., 2012) and higher concentrations of S on the surfaces of the needles forming the “pin-cushion” shaped nanoparticles (S-rich nano-domains), the compositional trend observed in this study could also be the result of two different processes: 1) a variation in the predominance of the HFO nano-domains within the sulfate rich amorphous matrix and 2) a coupled variation of the Fe and S content of the overall nanoparticles. The result of the predominance of each process (depending on the environment) and the possible interactions between them should determine the final bulk composition of each schwertmannite sample.

4.3. Thermodynamic model for the polyphasic nature of schwertmannite

Schwertmannite consists of three oxide components (Fe_2O_3, SO_3, and H_2O), which (according to Gibbs` phase rule) implies that at equilibrium three phases should coexist at a fixed temperature and pressure. Taking into account the recent discoveries reporting HFO and S-rich nano-domains within schwertmannite nanoparticles (Hockridge et al., 2009; French et al., 2012), it is assumed in this section that the three phases at equilibrium during schwertmannite precipitation are: a) schwertmannite (sch) accounting for the general behavior of schwertmannite and with the formula $Fe_8O_8(OH)_{8-2x}(SO_4)_x$; b) an HFO with a variable degree of hydration, represented by a nominal formula FeOOH and accounting for the HFO nano-domains in schwertmannite nanoparticles; and c) aqueous solution (soln).

The relationship between these three phases is complicated because they all have a variable composition and variable thermodynamic stability. Previous attempts to understand schwertmannite solubility considered only the reaction between the solution and schwertmannite but the model developed here satisfies the requirement that all three phases coexist at equilibrium. A $\log\left(a_{Fe^{3+}}/a^3_{H^+}\right)-\log\left(a^2_{H^+}a_{SO_4^{2-}}\right)$ diagram (Fig. 5) is used to illustrate this model. Three reactions define the three phase boundaries in this system.

(sch/soln) $Fe_8O_8(OH)_{8-2x}(SO_4)_x + (24-2x)H^+ = 8Fe^{3+} + xSO_4^{2-} + (16-2x)H_2O$ (2)

(HFO/soln) $FeOOH + 3H^+ = Fe^{3+} + 2H_2O$ (7)

(sch/HFO) $Fe_8O_8(OH)_{8-2x}(SO_4)_x + 2xH_2O = 8FeOOH + 2xH^+ + xSO_4^{2-}$ (8)

The equilibrium constants for these reactions are:

$$K_2 = \frac{a^8_{Fe^{3+}} a^x_{SO_4^{2-}}}{a^{24-2x}_{H^+}} = \left(\frac{a_{Fe^{3+}}}{a_{H^+}}\right)^8 \left(a^2_{H^+} \cdot a_{SO_4^{2-}}\right)^x \tag{9}$$

$$K_7 = \left(\frac{a_{Fe^{3+}}}{a_{H^+}}\right) \tag{10}$$

$$K_8 = \frac{K_2}{\left(K_7\right)^8} = \left(a^{2x}_{H^+} \cdot a^x_{SO_4^{2-}}\right) = \left(a^2_{H^+} \cdot a_{SO_4^{2-}}\right)^x \tag{11}$$

Algebraic manipulation of the log transformed equilibrium constant equations produce equations that describe the location of the phase boundaries on the activity diagram.

sch/soln: $$\log\left(\frac{a_{Fe^{3+}}}{a_{H^+}}\right) = \frac{1}{8}\log K_2 - \frac{x}{8}\log\left(a^2_{H^+} a_{SO_4^{2-}}\right) \tag{12}$$

HFO/soln: $$\log\left(\frac{a_{Fe^{3+}}}{a_{H^+}}\right) = \log K_7 \tag{13}$$

sch/HFO: $$\log\left(a^2_{H^+} a_{SO_4^{2-}}\right) = \frac{1}{x}\log K_8 \tag{14}$$

Inspection of these equations shows that because the sch/soln and sch/HFO boundaries change with changing schwertmannite composition (*x*), the HFO/soln boundary must also change as the schwertmannite pseudo-solid solution composition changes in order to satisfy the geometric constraints of the diagram. This means that the stability (solubility) of the HFO phase is a function of *x*.

Linear regression models were applied to the data in Table 1 to establish the correlations between *x* and log K_2, between $\log\left(a_{\mathrm{Fe}^{3+}} / a^3_{\mathrm{H}^+}\right)$ and log K_2, and between $\log\left(a^2_{\mathrm{H}^+} a_{\mathrm{SO}_4^{2-}}\right)$ and log K_2.

$$\log K_2 = 40.40(3.47) - 15.10(2.27)x \quad (n = 23,\ R^2 = 0.68) \tag{6}$$

$$\log\left(a_{\mathrm{Fe}^{3+}} / a^3_{\mathrm{H}^+}\right) = 1.905(0.190) + 0.1048(0.0102)\log K_2 \quad (n = 23,\ R^2 = 0.83) \tag{15}$$

$$\log\left(a^2_{\mathrm{H}^+}a_{\mathrm{SO}_4^{2-}}\right) = -5.879(0.388) - 0.1387(0.0208)\log K_2 \quad (n = 23,\ R^2 = 0.68) \qquad (16)$$

The numbers in parentheses are 1 standard error of the regression parameter. Log K_2 is already expressed in terms of x. Equation (15) can be combined with (6) to produce a relationship between log K_7 and x.

$$\log K_7 = \log\left(a_{\mathrm{Fe}^{3+}}/a^3_{\mathrm{H}^+}\right) = 6.139 - 1.582x \qquad (17)$$

Combining equation (16) with (6) gives a relationship between $\log\left(a^2_{\mathrm{H}^+}a_{\mathrm{SO}_4^{2-}}\right)$ and x.

$$\log\left(a^2_{\mathrm{H}^+}a_{\mathrm{SO}_4^{2-}}\right) = -11.48 + 2.094x \qquad (18)$$

This equation can be combined with (14) to get the relationship between log K_8 and x.

$$\log K_8 = -11.48x + 2.094x^2 \qquad (19)$$

Equation (6) can be combined with equation (12) to get an equation for the sch/soln line on the activity diagram (Fig. 5).

$$\log\left(a_{\mathrm{Fe}^{3+}}/a^3_{\mathrm{H}^+}\right) = 5.05 - x\left(1.89 + 0.125\log\left(a^2_{\mathrm{H}^+}a_{\mathrm{SO}_4^{2-}}\right)\right) \qquad (20)$$

The HFO/solution boundary is defined by equation (17) and the sch/HFO boundary is defined by combining equation (14) with (19).

$$\log\left(a^2_{H^+}a_{SO_4^{2-}}\right) = -\frac{11.48}{x} + 2.094 \qquad (21)$$

Figure 5 shows how the sch-HFO-soln triple point shifts as x changes from 1 to 2. Note that the slope of the sch-soln boundary changes from 0.125 to 0.250 as x changes from 1 to 2. This diagram shows that the solution compositions from Table 1 plot along the path of the triple point as required by the model. This activity diagram illustrates how the stability of schwertmannite and the stability of a coexisting hydrous ferric oxide are linked. This means that the solubility of schwertmannite and the coexisting HFO phase should be considered jointly. This can be done by combining equation (17) with equation (19) to produce an equation for the locus of points that defines the path of the triple point caused by changing x.

$$\log\left(a_{\mathrm{Fe}^{3+}} / a^{3}_{\mathrm{H}^+}\right) = -2.536 - 0.7555 \log\left(a^{2}_{\mathrm{H}^+} a_{\mathrm{SO}_4^{2-}}\right) \tag{22}$$

This equation compares favorably with the regression model based on the solution data in Table 1.

$$\log\left(a_{\mathrm{Fe}^{3+}} / a^{3}_{\mathrm{H}^+}\right) = -1.596(0.415) - 0.6426(0.0494)\log\left(a^{2}_{\mathrm{H}^+} a_{\mathrm{SO}_4^{2-}}\right)\ (n = 23,\ R^2 = 0.89) \tag{23}$$

The equations generated for this model, and synthesized in figure 4, predict that when $x = 1$, log $K_2 = 25.3$, log $K_7 = 4.56$, and log $K_8 = -9.39$, while when $x = 2$, log $K_2 = 10.2$, log $K_7 = 2.98$, and log $K_8 = -14.6$. As expected, the predicted values for schwertmannite solubility product within this model are consistent with the log K_{sp} range obtained in this study. In addition, the calculated values for the varying solubility products of the HFO phase (K_7) are in agreement with the solubility products commonly offered in the literature for ferrihydrite (K_{sp} from 2.47 to 10.27, Cornell and Schwertmann, 2003) while are a little bit higher than the reported values for goethite (K_{sp} from -0.43 to 2.17, Cornell and Schwertmann, 2003).

It might also be possible to estimate a value for x, if a schwertmannite sample is not available for analysis, by rearranging either equation (17) or (18), keeping in mind the uncertainties associated with the regression models.

Thermodynamic models provide valuable insights into how phase stability is related to phase composition but they are of limited value for predicting the physical situation of the phases. For example, the observed chemical behavior of the sch-HFO-soln system can be modeled using the phase stoichiometry for schwertmannite and HFO from equations (1) and (2) but another stoichiometry could be used as long as the element ratios in the chemical formulae are similar. Our model is consistent with the stoichiometry of sulfate-akaganéite as a model for schwertmannite but it places no constraints on the actual crystal structure of the mineral. Furthermore, our model requires that schwertmannite be in equilibrium with HFO as well as with solution but it cannot predict the amount or location of the HFO. This means that a complete understanding of schwertmannite paragenesis depends upon additional information from XRD, TEM, and related techniques.

5. Summary

On the basis of the results presented in this study, a new progressive and flexible solubility products range (from 5.8 to 39.5, as log K_{sp}) is proposed to better reproduce the complex solubility exhibited by schwertmannite in nature. A set of three different statistical predictive equations was obtained as a decision tool to generate the best log K_{sp} to be used in any specific environment. These equations allow one to obtain the most appropriate value for schwertmannite log K_{sp} in many Earth and planetary environments, even when information about the water chemistry or the solid composition is missing (e.g., absence of previous water chemistry on the surface of Mars or the lack of solid composition in certain studies modeling acidic waters).

A pe-pH predominance diagram for the main Fe mineral phases in the Fe-S-K-O-H system at 298 K and 1 bar was generated. The distribution and extension of the obtained predominance fields (reducing the preponderance of the goethite field and increasing schwertmannite and ferrihydrite predominance fields, compared to previous studies) reproduce in a more reliable way the neoformed mineralogy typically observed in AMD affected waters. This new pe-pH predominance diagram offers a realistic and intuitive tool to gain a general understanding of the main Fe mineral phase relationships and distributions in nature.

It was observed how Fe and S content in schwertmannite clearly defines a coupled decrease tendency for both elements, progressively moving from higher Fe and S concentrations to lower Fe and S concentrations. In addition, an increase in schwertmannite Fe/S molar ratio was observed coupled to a decrease in S concentration. This pseudo-solid solution behavior may be attributed to variations in the predominance of hydrous ferric oxide (HFO) and S-rich nano-domains within schwertmannite nanoparticles. The polyphasic nature of schwertmannite was also studied by means of a thermodynamic model. The initial assumption of equilibrium between two potential phases comprising schwertmannite nanoparticles (accounting for the HFO and S-rich nano-domains) and aqueous solution was supported by the results obtained in this model.

All the hydrochemical, compositional and thermodynamical results obtained in this study line up with the idea of the nano-polyphasic nature for schwertmannite and encourages using a broad log K_{sp} range to reproduce the solubility of schwertmannite in nature.

Acknowledgments

This study was funded by the Spanish Ministry of Science and Technology through project CTM2007-66724-C02/TECNO and by the Environmental Council of the Andalusia Regional Government. M.A.C. was financially supported by the Spanish Ministry of Education and the Post-doctoral International Mobility Sub-programme I+D+i 2008-2011

References

Acero, P., Ayora, C., Torrentó, C., Nieto, J. M., 2006. The behavior of trace elements during schwertmannite precipitation and subsequent transformation into goethite and jarosite. Geochimica et Cosmochimica Acta 70, 4130-4139.

Anbar, A. D., Duan, Y., Lyons, T. W., Arnold, G. L., Kendall, B., Creaser, R. A., Kaufman, A. J., Gordon, G. W., Scott ,C., Garvin, J., Buick, R., 2007. A whiff of oxygen before the great oxidation event? Science 317, 1903-1906.

Asta, M. P., Ayora, C., Román-Ross, G., Cama, J., Acero, P., Gault, A. G., Charnock, J. M., Bardelli, F., 2010. Natural attenuation of arsenic in the Tinto Santa Rosa acid stream (Iberian Pyritic Belt, SW Spain): The role of iron precipitates. Chemical Geology 271, 1-12.

Ball, J. W., Nordstrom, D. K., 1991. User's manual for WATEQ4F with revised thermodynamic database and test cases for calculating speciation of major, trace and redox elements in natural waters. US Geological Survey Water-Resources Investigations Reports, pp. 91–183.

Banfield, J. F., Zhang, H. Z., 2001. Nanoparticles in the environment. In Nanoparticles and the Environment (eds. Banfield J. F. and Navrotsky A.) Reviews in Mineralogy and Geochemistry, Mineralogical Society of America., Washington DC, USA. pp. 1-58.

Bibring, J. P., Arvidson, R. E., Gendrin, A., Gondet, B., Langevin, Y., Le Mouelic, S., Mangold, N., Morris, R. V., Mustard, J. F., Poulet ,F., Quantin, C., Sotin, C., 2007. Coupled ferric oxides and sulfates on the martian surface. Science 317, 1206-1210.

Bigham, J. M., Nordstrom, D. K., 2000. Iron and Aluminum Hydroxysulfates from Acid Sulfate Waters. In Sulfate Minerals: Crystallography, Geochemistry, and Environmental Significance (eds. Alpers C. N., Jambor J. L. and Nordstrom D. K.). Reviews in Mineralogy and Geochemistry, Mineralogical Society of America., Chantilly, Virginia. pp. 351-403.

Bigham, J. M., Schwertmann, U., Traina, S. J., Winland, R. L., Wolf, M., 1996. Schwertmannite and the chemical modeling of iron in acid sulfate waters. Geochimica et Cosmochimica Acta 60, 2111-2121.

Bigham, J. M., Carlson, L., Murad, E., 1994. Schwertmannite, a new iron oxyhydroxysulphate from Pyhasalmi, Finland, and other localities. Mineralogical Magazine 58, 641-648.

Burton, E. D., Bush, R. T., Sullivan, L. A., Mitchell, D. R. G., 2008. Schwertmannite transformation to goethite via the Fe(II) pathway: Reaction rates and implications for iron-sulfide formation. Geochimica et Cosmochimica Acta 72, 4551-4564.

Caraballo, M.A., Rotting, T.S., Nieto, J.M., Ayora, C., 2009. Sequential extraction and DXRD applicability to poorly crystalline Fe- and Al-phase characterization from an acid mine water passive remediation system. American Mineralogist, 94(7), 1029-1038.

Caraballo, M. A., Macías, F., Rötting, T. S., Nieto, J. M., Ayora, C., 2011. Long term remediation of highly polluted acid mine drainage: A sustainable approach to restore the environmental quality of the Odiel river basin. Environmental Pollution 159, 3613-3619.

Cornell, R. M., Schwertmann, U., 2003. The iron oxides: structure, properties, reactions, occurrences and uses. WILEY-VCH, Weinheim.

Farrand, W. H., Glotch, T. D., Rice Jr, J. W., Hurowitz, J. A., Swayze, G. A., 2009. Discovery of jarosite within the Mawrth Vallis region of Mars: Implications for the geologic history of the region. Icarus 204, 478-488.

Fernández-Martínez, A., Timon, V., Román-Ross, G., Cuello, G. J., Daniels, J. E., Ayora, C., 2010. The structure of schwertmannite, a nanocrystalline iron oxyhydroxysulfate. American Mineralogist 95, 1312-1322.

French, R. A., Caraballo, M. A., Kim, B., Rimstidt, J. D., Murayama, M., Hochella, M. F., 2012. The enigmatic iron oxyhydroxylsulfate nanomineral schwertmannite: Morphology, structure and composition. American Mineralogist 97, 1469-1482.

Hassellov, M., von der Kammer, F., 2008. Iron Oxides as Geochemical Nanovectors for Metal Transport in Soil-River Systems. Elements 4, 401-406.

Hoashi, M., Bevacqua, D. C., Otake, T., Watanabe, Y., Hickman, A. H., Utsunomiya, S., Ohmoto, H., 2009. Primary haematite formation in an oxygenated sea 3.46 billion years ago. Nature Geoscience 2, 301-306.

Hockridge, J. G., Jones, F., Loan, M., Richmond, W. R., 2009. An electron microscopy study of the crystal growth of schwertmannite needles through oriented aggregation of goethite nanocrystals. Journal of Crystal Growth 311, 3876-3882.

Hurowitz, J. A., Fischer, W. W., Tosca, N. J., Milliken, R. E., 2010. Origin of acidic surface waters and the evolutionof atmospheric chemistry on early Mars. Nature Geoscience 3, 323-326.

Johnston, S. G., Keene, A. F., Bush, R. T., Burton, E. D., Sullivan, L. A., Isaacson, L., McElnea, A. E., Ahern, C. R., Smith, C. D., Powell, B., 2011. Iron geochemical zonation in a tidally inundated acid sulfate soil wetland. Chemical Geology 280, 257-270.

Kawano, M., Tomita, K., 2001. Geochemical modeling of bacterially induced mineralization of schwertmannite and jarosite in sulfuric acid spring water. American Mineralogist 86, 1156-1165.

Konhauser, K. O., Lalonde ,S. V., Planavsky, N. J., Pecoits, E., Lyons, T. W., Mojzsis, S. J., Rouxel, O. J., Barley, M. E., Rosíere, C., Fralick, P. W., Kump, L. R., Bekker, A., 2011. Aerobic bacterial pyrite oxidation and acid rock drainage during the Great Oxidation Event. Nature 478, 369-373.

Konhauser, K. O., Pecoits, E., Lalonde, S. V., Papineau, D., Nisbet, E. G., Barley, M. E., Arndt, N. T., Zahnle, K., Kamber, B. S., 2009. Oceanic nickel depletion and a methanogen famine before the Great Oxidation Event. Nature 458, 750-753.

Li ,D. S., Nielsen, M. H., Lee, J. R. I., Frandsen, C., Banfield, J. F., De Yoreo, J. J., 2012. Direction-Specific Interactions Control Crystal Growth by Oriented Attachment. Science 336, 1014-1018.

Macías, F., Caraballo, M. A., Nieto, J. M., Rötting, T.S., Ayora, C., 2012. Natural pretreatment and passive remediation of highly polluted acid mine drainage. Journal of Environmental Management 104, 93-100.

Madden, A. S., Hochella Jr., M. F., 2005. A test of geochemical reactivity as a function of mineral size: Manganese oxidation promoted by hematite nanoparticles. Geochimica et Cosmochimica Acta 69, 389-398.

Majzlan ,J., Navrotsky, A., Schwertmann, U., 2004. Thermodynamics of iron oxides: Part III. Enthalpies of formation and stability of ferrihydrite (~Fe(OH)3), schwertmannite (~FeO(OH)3/4(SO4)1/8), and ve-Fe2O3. Geochimica Cosmochimica Acta 68, 1049-1059.

Marion, G. M., Kargel, J. S., Catling, D. C., 2008. Modeling ferrous-ferric iron chemistry with application to martian surface geochemistry. Geochimica et Cosmochimica Acta 72, 242-266.

Navrotsky, A., Mazeina, L., Majzlan, J., 2008. Size-driven structural and thermodynamic complexity in iron oxides. Science 319, 1635-1638.

Nocete, F., Álex, E., Nieto, J. M., Sáez, R., Bayona, M. R., 2005. An archaeological approach to regional environmental pollution in the south-western Iberian Peninsula related to Third millennium BC mining and metallurgy. Journal of Archaeological Science 32, 1566-1576.

Parkhurst, D.L., 1995. User's guide to PHREEQC: a computer program for speciation,reaction path, advective-transport, and inverse geochemical calculations. US Geological Survey Water-Resources Investigations Reports pp. 95-4227.

Plathe, K.L., von der Kammer, F., Hassellov, M., Moore, J.N., Murayama, M., Hofmann, T., Hochella Jr., M.F., 2013. The role of nanominerals and mineral nanoparticles in the transport of toxic trace metals: Field-flow fractionation and analytical TEM analyses after nanoparticle isolation and density separation. Geochimica et Cosmochimica Acta 102, 213-225.

Raiswell, R., Benning, L. G., Davidson, L., Tranter, M., Tulaczyk, S., 2009. Schwertmannite in wet, acid, and oxic microenvironments beneath polar and polythermal glaciers. Geology 37, 431-434.

Regenspurg, S., Brand, A., Peiffer, S., 2004. Formation and stability of schwertmannite in acidic mining lakes. Geochimica et Cosmochimica Acta 68, 1185-1197.

Sánchez España, J., López Pamo, E., Santofimia, E., Aduvire, O., Réyes, J., Barettino, D., 2005. Acid mine drainage in the Iberian Pyrite Belt (Odiel river watershed, Huelva, SW Spain): Geochemistry, mineralogy and environmental implications. Applied Geochemistry 20, 1320-1356.

Sarmiento, A. M., Nieto, J. M., Olías, M., Cánovas, C. R., 2009. Hydrochemical characteristics and seasonal influence on the pollution by acid mine drainage in the Odiel river Basin (SW Spain). Applied Geochemistry 24, 697-714.

Sidenko, N. V., Sherriff, B. L., 2005. The attenuation of Ni, Zn and Cu, by secondary Fe phases of different crystallinity from surface and ground water of two sulfide mine tailings in Manitoba, Canada. Applied Geochemistry 20, 1180-1194.

Tosca, N. J., Knoll, A. H., McLennan, S. M., 2008. Water activity and the challenge for life on early mars. Science 320, 1204-1207.

Tyler, G., Carrasco, R., Nieto ,J.M., Pérez, R., Ruiz, M.J., Sarmiento, A.M., 2004. Optimization of Mayor and Trace Element Determination on Acid Mine Drainage samples by Ultrasonic Nebulizer-ICP-OES (USN-ICP-OES) In Pittcon Conference 7-12 March Chicago, USA.

West, L., McGown, D. J., Onstott, T. C., Morris, R. V., Suchecki, P., Pratt, L. M., 2009. High Lake gossan deposit: An Arctic analogue for ancient Martian surficial processes? Planetary Space Science 57, 1302-1311.

Yu, J. Y., Heo, B., Choi, I. K., Cho, J. P., Chang, H. W., 1999. Apparent solubilities of schwertmannite and ferrihydrite in natural stream waters polluted by mine drainage. Geochimica et Cosmochimica Acta 63, 3407-3416.

Yu, J. Y., Heo, B., 2001. Dilution and removal of dissolved metals from acid mine drainage along Imgok Creek, Korea. Applied Geochemistry 16, 1041-1053.

Figure legends

Figure 1. X-ray diffraction patterns for the 9 pure natural schwertmannite samples collected at the Iberian Pyrite Belt. The first three samples (red) were obtained at the Tinto basin whereas the six last samples (blue) belongs to AMDs at the Odiel Basin. TCT1-2 =

Tinto Cabecera del Tinto 1 and 2, TB = Tinto Berrocal, OA = Odiel Agrio, OC = Odiel Cueva, OE = Odiel Esperanza, OTSR1-2 = Odiel Tinto Santa Rosa 1 and 2, and O5O = Odiel 5 Ojos. All the diffractograms are shown using 2400 counts as the maximum value for the y-axis.

Figure 2. Statistical distribution of the main variates involved in natural schwertmannite formation. The three first histograms (from top to bottom) were calculated using the information in Table 1 (n = 30) whereas the histogram corresponding to schwertmannite Fe/S_{molar} ratio was obtained using the information in Table A1.

Figure 3. A) Graphical trend between S and Fe content in 46 natural schwertmannite samples. The dashed lines correspond to the 95% confidence interval for the regression line fitted. B) Graphical trend between S content and Fe/S molar ratio in natural schwertmannite. The expansion from the traditional Fe/S_{molar} range (from 4 to 8) to the broader range proposed in the current study (from 3.77 to 15.52) is graphically shown. Concentrations are given in mol of element (Fe or S) per g of schwertmannite.

Figure 4. All the diagrams are for Fe-S-K-O-H system at 298 K and 1 bar. **A)** pe-pH predominance diagram for the stable Fe mineral phases. **B)** pe-pH predominance diagram for the meta-stable Fe mineral phases. **C)** Final pe-pH predominance diagram for stable and meta-stable Fe mineral phases obtained after overlapping the information shown in A and B. Abbreviations: Fe^{3+}, Fe^{2+}, SO_4^{2-}, HSO_4^- and H_2O = dissolved species; H_2 and O_2 = gas species; jr = jarosite; schw = schwertmannite; gt = goethite; fh = ferrihydrite and py = pyrite. Dashed lines are employed to delimit the predominance fields of the metastable phases (schw and fh). Square symbols correspond to field samples from the Iberian Pyrite Belt, circle symbols stands for "bibliographic" natural samples.

Figure 5. Natural schwertmannite samples distribution in the space defined by $\log\left(a_{Fe^{3+}}/a_{H^+}^3\right)$ versus $\log\left(a_{H^+}^2 a_{SO_4^{2-}}\right)$ and location of the predominance fields in the schw/HFO/soln system for two extreme compositions of schwertmannite (x = 1 and 2).

The dashed line is the regression model for the measured values. HFO = hydrous ferric oxide, sch = schwertmannite and soln = solution.

Figure 1

Fig.1

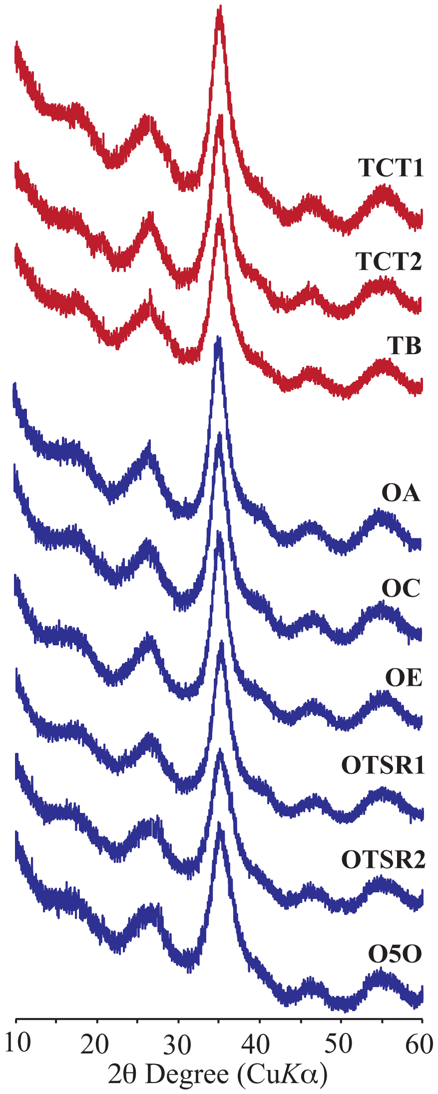

Figure 2

Fig.2

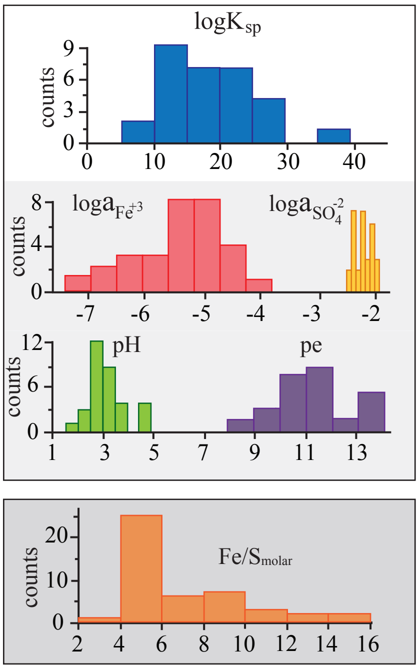

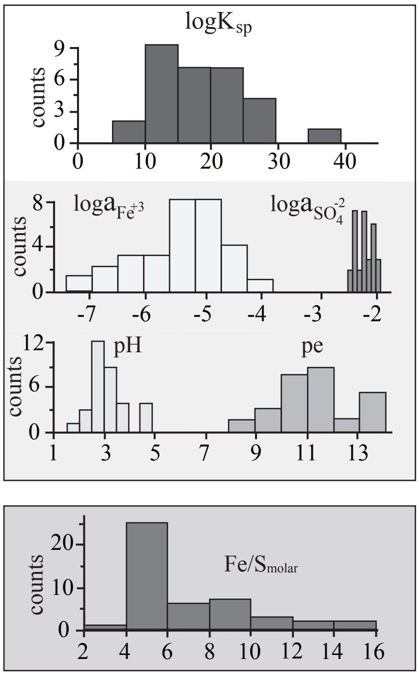

Figure 3

Fig.3

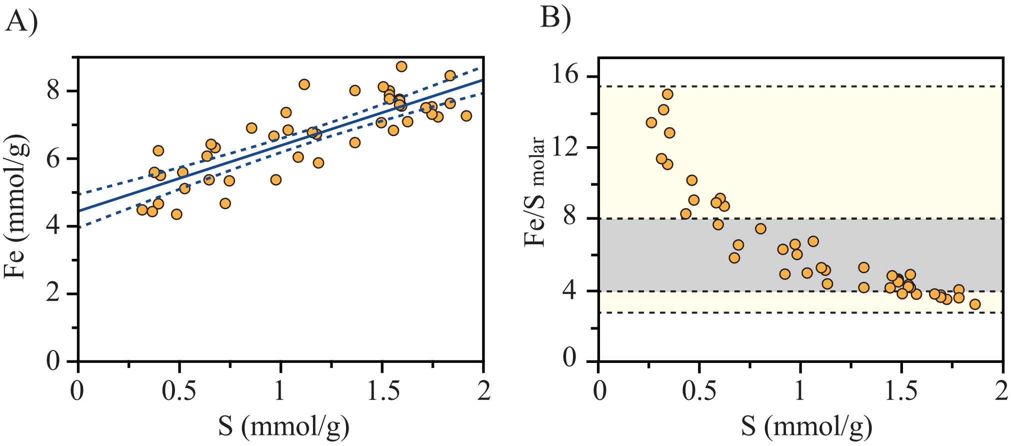

Figure 4

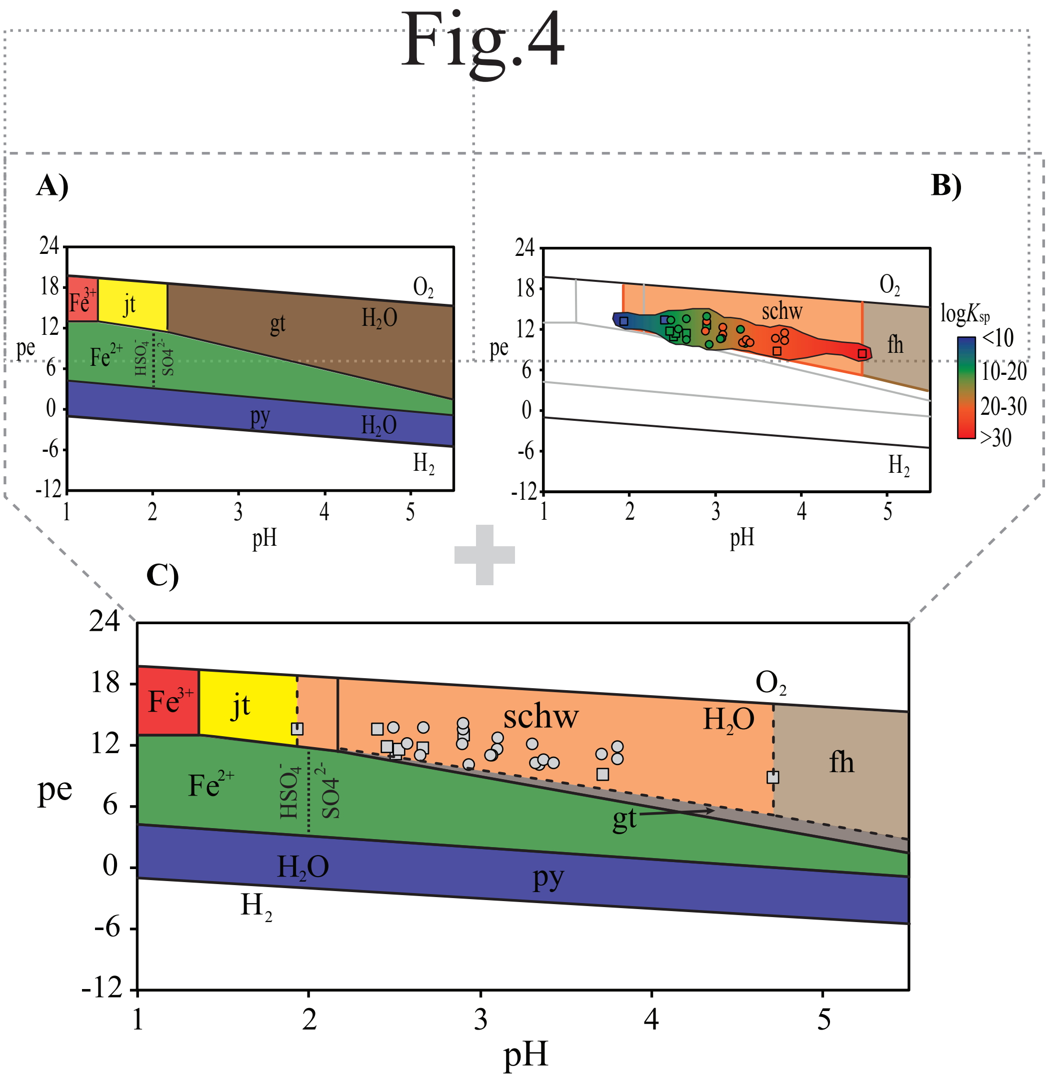
Fig.4
A)
B)
C)
pe
pH
24
18
12
6
0
-6
-12
1
2
3
4
5
Fe^{3+}
jt
gt
H_2O
O_2
Fe^{2+}
HSO_4^-
$SO4^{2-}$
py
H_2
schw
fh
$\log K_{sp}$
<10
10-20
20-30
>30

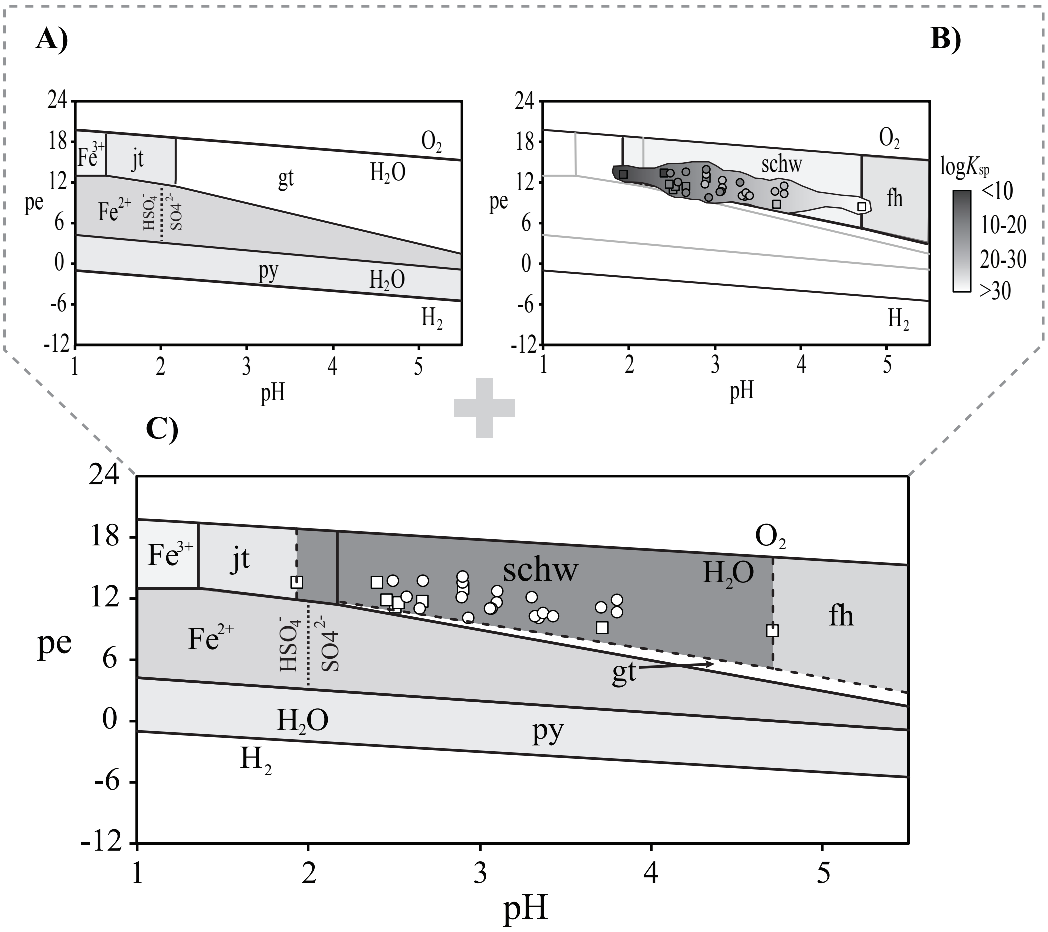
A)
B)
C)
pe
pH
24
18
12
6
0
-6
-12
1
2
3
4
5
Fe^{3+}
jt
gt
H_2O
O_2
Fe^{2+}
HSO_4^-
$SO4^{2-}$
py
H_2
schw
fh
$\log K_{sp}$
<10
10-20
20-30
>30

Fig.5

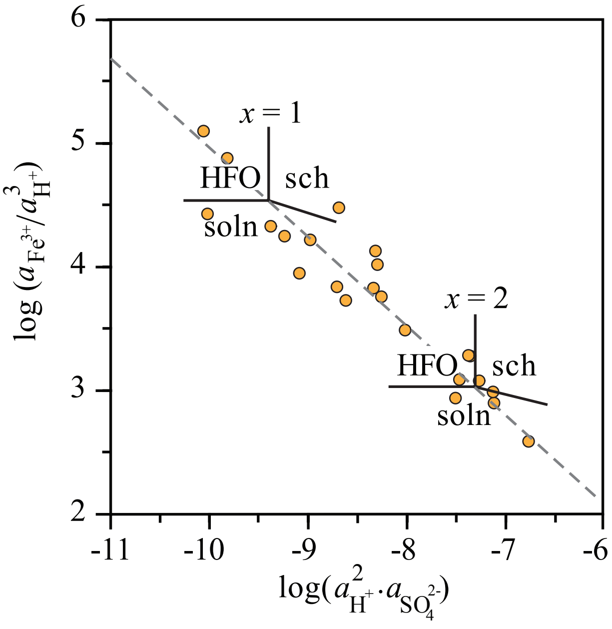
6
5
4
3
2
-11
-10
-9
-8
-7
-6
$x = 1$
HFO
sch
soln
$x = 2$
HFO
sch
soln
$\log(a_{Fe^{3+}}/a^3_{H^+})$
$\log(a^2_{H^+} \cdot a_{SO_4^{2-}})$

Table 1

Table 1. Summary of the water chemistry, solid composition and calculated logK_{sp} for the different schwertmannites covered in this study

	Water chemistry								Solid				
Location	pH	pe	Fe (mmol/L)	SO_4^{-2}(mmol/L)	loga_{Fe+3}	loga_{Fe+2}	loga_{SO4-2}	loga_{K+}	Fe (mmol/g)	S (mmol/g)	xSO_4^{-2}	Fe/S molar	logK_{sp}
Spain (TCT1)	4.71	8.50	14.11	56.37	-7.06	-2.54	-1.97	-	8.10	1.51	1.49	5.36	39.5*
Spain (TCT2)	3.71	8.80	12.34	54.09	-6.80	-2.58	-1.96	-4.45	7.99	1.37	1.37	5.85	21.8*
Spain (TB)	1.93	13.20	16.92	54.28	-3.81	-3.99	-2.24	-	7.69	1.59	1.66	4.83	5.8*
Spain (OA)	2.4	13.20	5.32	97.34	-4.61	-4.79	-1.97	-4.09	7.21	1.78	1.97	4.06	7.4*
Spain (OC)	2.66	11.40	3.60	35.48	-4.89	-3.27	-2.15	-4.22	6.45	1.37	1.70	4.70	12.0*
Spain (OE)	2.51	10.90	15.61	41.00	-4.63	-2.51	-2.10	-3.75	7.98	1.54	1.55	5.17	12.2*
Spain (OTSR1)	2.53	11.20	10.17	28.17	-4.51	-2.69	-2.21	-	7.73	1.59	1.64	4.87	12.7*
Spain (OTSR2)	2.45	11.50	9.38	28.29	-4.36	-2.84	-2.23	-4.63	7.86	1.54	1.57	5.10	12.8*
Spain (O5O)	2.9	12.60	0.73	26.39	-5.21	-4.79	-2.22	-4.41	7.74	1.54	1.60	5.02	15.1*
Spain	3.07	10.80	5.09	32.72	-5.19	-2.94	-2.16	-4.64	6.81	1.56	1.83	4.36	16.9$^{(1)}$
Spain	2.93	9.80	15.13	37.71	-5.63	-2.43	-2.09	-4.02	11.07	1.13	0.82	9.82	18.8$^{(2)}$
Spain	3.32	9.90	18.89	43.41	-5.48	-2.36	-2.05	-4.44	10.60	1.05	0.80	10.06	28.9$^{(2)}$
Spain	3.42	10.30	17.84	41.91	-5.06	-2.43	-2.02	-4.23	7.53	1.60	1.70	4.71	28.9$^{(2)}$
S. Korea	2.65	10.70	7.56	26.71	-5.01	-2.72	-2.21	-4.81	8.43	1.84	1.74	4.59	10.5$^{(3)}$
S. Korea	2.57	11.90	5.34	26.82	-4.43	-3.34	-2.22	-4.63	7.48	1.72	1.84	4.34	12.7$^{(3)}$
S. Korea	3.34	9.90	2.69	10.92	-6.07	-2.99	-2.41	-4.60	7.29	1.75	1.92	4.17	14.2$^{(3)}$
Spain	3.3	11.70	0.33	13.01	-5.68	-4.32	-2.38	-4.48	7.56	1.59	1.68	4.76	18.7$^{(4)}$
Canada	2.49	13.40	6.09	44.97	-4.41	-4.74	-2.08	-3.22	5.57	0.52	0.75	10.62	19.2$^{(5)}$
Canada	3.09	11.30	1.15	26.34	-5.44	-3.74	-2.16	-4.08	5.32	0.75	1.13	7.10	21.3$^{(5)}$
Canada	2.66	13.40	1.77	31.27	-4.96	-5.29	-2.05	-3.43	5.35	0.65	0.97	8.23	17.0$^{(5)}$
S. Korea	2.57	11.90	5.34	26.82	-4.43	-3.34	-2.22	-4.63	7.07	1.63	1.84	4.35	12.7$^{(6)}$
Japan	3.37	10.20	2.24	9.69	-5.87	-3.05	-2.50	-3.70	-	-	1.32	6.06	21.7$^{(7)}$
Japan	3.06	10.80	1.52	9.84	-5.45	-3.27	-2.50	-3.70	-	-	1.05	7.62	20.8$^{(7)}$
Japan	2.89	11.80	1.22	10.77	-4.91	-3.70	-2.48	-3.66	-	-	1.05	7.62	21.4$^{(7)}$

Table 1. Continuation

	Water chemistry								Solid				
Location	pH	pe	Fe (mmol/L)	SO_4^{-2}(mmol/L)	$\log a_{Fe+3}$	$\log a_{Fe+2}$	$\log a_{SO4-2}$	$\log a_{K+}$	Fe (mmol/g)	S (mmol/g)	xSO_4^{-2}	Fe/S molar	$\log K_{sp}$
Germany	2.90	13.33	1.53	8.50	-4.57	-4.89	-2.52	-	-	-	1.36	5.90	21.7(8)
Germany	3.10	12.40	0.22	7.40	-5.46	-	-2.51	-3.61	-	-	1.70	4.70	15.9(8)
Germany	2.90	13.70	1.22	19.40	-4.80	-	-2.40	-4.06	-	-	2.58	3.10	10.0(8)
USA	3.80	11.50	0.03	10.66	-6.98	-5.46	-2.42	-5.46	-	-	1.18	6.80	23.6(9)
USA	3.70	10.65	0.47	9.38	-6.22	-3.85	-2.42	-3.85	-	-	1.23	6.50	26.9(9)
USA	3.80	10.38	0.64	8.08	-6.30	-3.66	-2.46	-3.66	-	-	1.43	5.60	26.4(9)
Quantiles													
90%	3.79	13.39	16.79	54.26	-4.41	-2.43	-1.96	-3.56	10.17	1.77	1.91	9.66	28.7
75%	3.35	12.45	10.71	41.23	-4.60	-2.70	-2.09	-3.70	7.99	1.62	1.71	6.88	21.7
50%	2.92	11.35	4.35	26.82	-5.13	-3.31	-2.22	-4.16	7.56	1.54	1.56	5.14	17.9
25%	2.57	10.36	1.20	10.74	-5.73	-4.24	-2.42	-4.61	6.94	1.25	1.17	4.67	12.7
10%	2.45	9.81	0.34	8.59	-6.75	-4.93	-2.50	-4.70	5.30	0.67	0.84	4.19	10.1
Maximum	4.71	13.70	18.89	97.34	-3.81	-2.36	-1.96	-3.22	11.07	1.84	2.58	10.62	39.5
Minimum	1.93	8.50	0.03	7.40	-7.06	-5.46	-2.52	-5.46	5.32	0.52	0.75	3.10	5.8
Mean	3.02	11.37	-	-	-5.27	-	-2.24	-4.17	-	-	1.48	-	18.3
Std. Dev.	0.56	1.37	-	-	0.82	-	0.18	0.51	-	-	0.40	-	7.3

*This study: TCT1 = Tinto Cabecera del Tinto 1, TCT2 = Tinto Cabecera Tinto 2, TB = Tinto Berrocal, OA = Odiel Agrio, OC = Odiel Cueva, OE = Odiel Esperanza, OTSR1 = Odiel Tinto Santa Rosa 1, OTSR2 = Odiel Tinto Santa Rosa 2, O5O = Odiel 5 Ojos.

(1) Acero et al., 2006; (2) Asta et al., 2010; (3) Yu et al., 1999; (4) Sánchez-España et al., 2005; (5) Sidenko and Sherriff, 2005; (6) Yu and Heo, 2001; (7) Kawano and Tomita, 2001; (8) Regenspurg et al., 2004 and (9) Bigham et al., 1996.

$\log a_{Fe+3}$ and $\log a_{SO4-2}$= logarithms of the ferric iron and sulfate activities in the waters generating schwertmannite; xSO_4^{-2}= schwertmannite stoichiometric sulfate; $\log K_{sp}$ = solubility product constant calculated for schwertmannite.

Mean and standard deviation (Std. Dev.) were only shown when the dataset displayed a normal distribution. Normality was tested by the visual inspection of the Normal Quantile Plot as well as fitting a line to the data distribution and checking the Goodness of fit of this line to a normal distribution.

Table 2

Table 2. Reproducibility in % of the modeled log K_{sp} values

Location	log K_{sp}	m-log K_{sp}	(%)	w-log K_{sp}	(%)	s-log K_{sp}	(%)
Spain*	12.2	12.29	100.8	12.66	103.8	17.03	139.6
Spain*	7.4	6.94	93.8	11.11	150.2	10.63	143.7
Spain*	12.0	11.96	99.7	13.77	114.8	14.67	122.3
Spain*	5.8	5.48	94.5	5.81	100.2	15.40	265.4
Spain*	39.5	40.21	101.8	41.37	104.7	17.85	45.2
Spain*	15.1	15.22	100.8	16.27	107.8	16.32	108.1
Spain*	12.7	12.70	100.0	13.34	105.0	15.61	122.9
Spain*	12.8	12.86	100.5	12.68	99.0	16.73	130.7
Spain*	21.8	21.82	100.1	23.42	107.4	19.74	90.6
Spain(1)	16.9	17.29	102.3	19.96	118.1	12.71	75.2
Spain(2)	18.8	18.86	100.3	14.80	78.7	28.10	149.5
Spain(2)	28.9	28.80	99.7	23.53	81.4	28.40	98.3
Spain(2)	28.9	27.33	94.6	28.17	97.5	14.75	51.0
S. Korea(3)	10.5	10.39	99.0	12.68	120.8	14.08	134.1
S. Korea(3)	12.7	12.64	99.6	14.61	115.0	12.55	98.8
S. Korea(3)	14.2	14.63	103.1	18.96	133.5	11.42	80.4
Spain(4)	18.7	18.99	101.5	20.66	110.5	15.04	80.4
Canada(5)	19.2	20.07	104.5	13.70	71.4	29.04	151.2
Canada(5)	21.3	21.32	100.1	18.86	88.5	23.40	109.8
Canada(5)	17.0	17.48	102.8	13.77	81.0	25.74	151.4
S. Korea(6)	12.7	12.68	99.9	14.61	115.0	12.61	99.3
Japan(7)	21.7	21.57	99.4	20.43	94.2	20.47	94.3
Japan(7)	20.8	20.54	98.8	16.96	81.5	24.55	118.0
Japan(7)	21.4	21.39	99.9	16.97	79.3	24.55	114.7
Germany(8)	21.7	21.91	100.9	19.10	88.0	19.93	91.8
Germany(8)	15.9	16.07	101.1	17.60	110.7	14.70	92.4
Germany(8)	10.0	10.46	104.6	18.12	181.2	1.42	14.2
USA(9)	23.6	22.90	97.0	22.38	94.8	22.64	95.9
USA(9)	26.9	26.60	98.9	25.02	93.0	21.82	81.1
USA(9)	26.4	26.47	100.3	26.38	99.9	18.83	71.3

*This study; (1) Acero et al., 2006; (2) Asta et al., 2010; (3) Yu et al., 1999; (4) Sánchez-España et al., 2005; (5) Sidenko and Sherriff, 2005; (6) Yu and Heo, 2001; (7) Kawano and Tomita, 2001; (8) Regenspurg et al., 2004 and (9) Bigham et al., 1996.

logK_{sp}, m-logK_{sp}, w-logK_{sp} and s-logK_{sp} = calculated, general model, w-model and s-model solubility product constant